Joule

CellPress

Article

Metal-organic frameworks for nanoconfinement of chlorine in rechargeable lithium-chlorine batteries

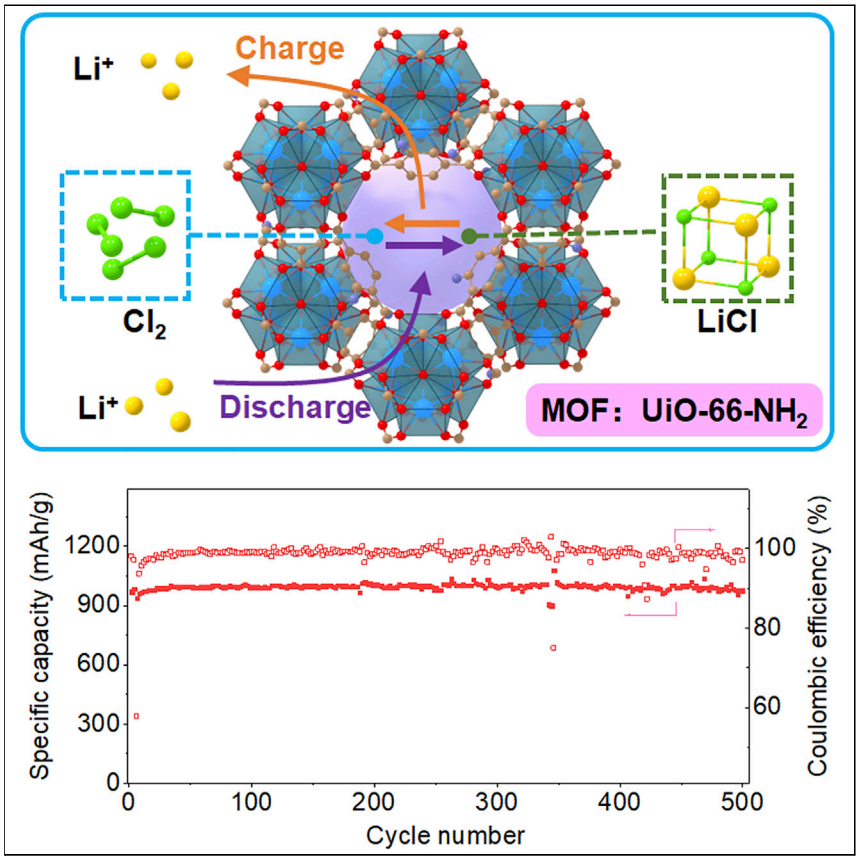

Rechargeable Li-Cl_2 batteries are an emerging and promising high-energy battery technology. We develop metal-organic frameworks (MOFs) with functional groups for the nanoconfinement of chlorine by chemisorption in the Li-Cl_2 battery. The functional MOFs boost the storage capability of Cl_2 and LiCl, contributing to excellent electrochemical performance for the Li-Cl_2 battery in a wide temperature range. The charge storage mechanism of the functional MOFs is revealed by a combination of low-dose HRTEM, cryo-TEM, and XPS.

Yan Xu, Long Jiao, Jiale Ma, ..., Zhenyu Li, Hai-Long Jiang, Wei Chen

zyli@ustc.edu.cn (Z.L.)
jianglab@ustc.edu.cn (H.-L.J.)
weichen1@ustc.edu.cn (W.C.)

Highlights

Metal-organic frameworks with functional groups are developed for Li-Cl_2 batteries

The Li-Cl_2 battery exhibits good electrochemical performance at both room and low temperatures

The storage mechanism of Cl_2 is studied by low-dose TEM and cryo-TEM

Xu et al., Joule 7, 515–528
March 15, 2023 © 2023 Elsevier Inc.
https://doi.org/10.1016/j.joule.2023.02.010

Joule

CellPress

Article

Metal-organic frameworks for nanoconfinement of chlorine in rechargeable lithium-chlorine batteries

Yan Xu,[1] Long Jiao,[2] Jiale Ma,[3] Pan Zhang,[4] Yongfu Tang,[4] Lingmei Liu,[5] Ying Liu,[5] Honghe Ding,[6] Jifei Sun,[1] Mingming Wang,[1] Zhenyu Li,[2,3,*] Hai-Long Jiang,[2,*] and Wei Chen[1,7,*]

SUMMARY

Metal-organic frameworks (MOFs) with functional groups are developed for the nanoconfinement of chlorine by chemisorption in a rechargeable Li-Cl_2 battery. Predicted by theoretical calculations, highly porous MOF functionalized with –NH_2 groups, namely UiO-66-NH_2, is screened out as a model to apply in the Li-Cl_2 battery. The Li-Cl_2 battery using NH_2-functionalized MOF (Li-Cl_2@MOF) demonstrates high specific capacities of up to 2,000 mAh/g and is highly stable for 500 cycles under a specific capacity of 1,000 mAh/g at room temperature. It also exhibits superior low-temperature performance, displaying a high voltage of 3.5 V and a Coulombic efficiency (CE) of 99.7% with 300 stable cycles under a capacity of 1,000 mAh/g at −25°C. Furthermore, the Li-Cl_2@MOF cell exhibits a high areal capacity of 4.4 mAh/cm^2 in coin cells and a CE of 99% for over 120 cycles in large-scale pouch cells. This work provides opportunities for the promising application of functionalized MOFs as cathodes in rechargeable Li-Cl_2 batteries.

INTRODUCTION

The development of high-energy batteries is highly desirable for meeting the ever-growing demand for energy storage.[1–3] Rechargeable Li-Cl_2 batteries were developed by Dai et al. in 2021 based on primary lithium-thionyl chloride (Li-$SOCl_2$) batteries, which delivered a high specific capacity of 1,200 mAh/g and a high output voltage of ~3.6 V, and considered one of the cutting-edge battery energy storage systems.[4] A rechargeable Li-Cl_2 battery typically consists of a Li metal anode, a $SOCl_2$-based nonaqueous electrolyte, and a Cl_2 storage cathode material, such as microporous carbon with a high surface area[4] and graphite flakes with tunnels.[5] The solid product of LiCl is generated on the cathode during the discharge process in Li-Cl_2 cell, which is oxidized to Cl_2 during the recharge process. Recently, other halogen cells, such as Na-Cl_2[5] and K-Br_2 cells,[6] have been developed. We take the Li-Cl_2 cell as the research target due to its high energy density among the halogen cells. However, several challenges need to be overcome to realize the practical application of the Li-Cl_2 cells. First, the supply of Cl_2 to the reaction is limited due to the weak physical adsorption of porous carbon to Cl_2 molecules. Second, the excessive generation of LiCl into the carbon pores tends to block the tunnels for Li^+ transportation and Cl_2 diffusion, impeding further electrochemical reactions. In addition, the shuttle effect of unbonded Cl_2 can cause battery decay, particularly at a high output capacity. Therefore, the cathode materials with highly porous structures are critical to overcome the above issues concerning the Li-Cl_2 batteries.

CONTEXT & SCALE

Rechargeable Li-Cl_2 batteries are considered one of the cutting-edge battery energy storage systems. We propose and demonstrate metal-organic frameworks (MOFs) with functional groups to facilitate the storage of Cl_2 by chemisorption in the Li-Cl_2 battery. The designed Li-Cl_2@MOF battery delivers high specific capacities up to 2,000 mAh/g with excellent rate capability and cycle stability. Even at low temperatures, it still exhibits a high voltage of 3.5 V and a CE of 99.7% with 300 stable cycles under a capacity of 1,000 mAh/g. Low-dose high-resolution transmission electron microscopy, cryogenic transmission electron microscopy, and X-ray photoelectron spectroscopy are utilized to reveal the storage mechanism on nanoconfinement of Cl_2 and LiCl by the functionalized MOFs in the Li-Cl_2@MOF battery.

Further improvements can be made by modification of the pore structures with polarities that can interact with Cl atoms.

Metal-organic frameworks (MOFs) with high porosity and versatile functionalities have been applied in various battery systems to improve their electrochemical performance.[7–12] The tuning of pore size, geometry, and chemical functionality of MOFs can realize many targeted applications, such as gas storage and separation for Li-air battery,[4,13–15] and shuttle effect suppression for Li-S batteries.[16–23] For example, Li et al. reported that MOFs with rich defects could lead to a significant oxygen enrichment in the framework.[13] Tarascon et al. demonstrated a mesoporous MOF with polarized surfaces, where mesopores with small apertures could suppress the migration of polysulfide species in Li-S batteries.[20] Compared with porous carbon materials, MOFs possess several distinct advantages,[24–27] including high porosity with uniform pores, adjustable pore sizes, and controllable functionalization of the organic linkers. The functionalized organic linkers make MOFs having a high affinity to some specific gases. For example, Lu et al. demonstrated that the introduction of $–NH_2$ groups in CAU-1-NH_2 MOF has successfully improved the capability of CO_2 capture in Li-air battery.[28] Yaghi et al. also verified the capture capability of $–NH_2$ groups of CAU-1-NH_2@polydopamine MOF to CO_2 molecules.[29] Inspired by the successful application of MOFs in Li-air battery, we speculate that MOFs may be potential good candidates for the cathode Cl_2/LiCl reactions in the Li-Cl_2 battery. One of the critical enablers of using MOFs in Li-Cl_2 battery is to design MOFs with high porosity and functional groups for the confinement of LiCl and Cl_2. Considering that both LiCl and Cl_2 are Lewis acids, we further speculate that MOFs constructed by organic ligands with Lewis basic functional groups may be promising candidates for the storage of LiCl and Cl_2.

In this work, we propose to apply highly porous MOFs with Lewis basic functional groups in Li-Cl_2 batteries to improve the Cl_2/LiCl conversion reactions. Guided by the theoretical prediction using first-principles calculations, MOFs with $–NH_2$ functional groups are screened out for the applications in the Li-Cl_2 battery (referred to as Li-Cl_2@MOF battery). It is revealed by cryo-TEM and low-dose high-resolution TEM (HRTEM) that UiO-66-NH_2 is stable during cycling, and XPS verify the strong affinity of the $–NH_2$ groups to Cl_2 and LiCl, thereby boosting their redox reaction kinetics. Our designed Li-Cl_2@MOF cell delivers a highly rechargeable specific capacity of up to 2,000 mAh/g and is stable over 500 cycles under a high capacity of 1,000 mAh/g. Moreover, the Li-Cl_2 cell exhibits excellent low-temperature electrochemical performance down to −40°C, as well as high areal capacities in coin cells and extended capacities in large-scale pouch cells, demonstrating its practical energy storage applications. This work demonstrates that functional MOFs can provide an innovative pathway to the performance improvement of rechargeable Li-Cl_2 batteries.

RESULTS AND DISCUSSION

Prediction of $–NH_2$ groups functionalized MOFs for Li-Cl_2 batteries

We screened a series of MOFs for deployment in the Li-Cl_2 battery. Given the electrochemical stability, Zr-based MOF was chosen as the main framework in our work. Furthermore, considering the synthetic availability, UiO-66 MOF was used as the base MOF. We then carried out density functional theory (DFT)-based first-principles calculations to determine the adsorption energy of Cl atom on several Lewis base groups, including $–NH_2$, –Cl, –OH, and $–OCH_3$ groups. As shown in Figures 1A and S1, the adsorption energies of UiO-66, UiO-66-NH_2, UiO-66-Cl, UiO-66-OH,

[1]Department of Applied Chemistry, School of Chemistry and Materials Science, Hefei National Research Center for Physical Sciences at the Microscale, University of Science and Technology of China, Hefei, Anhui 230026, China

[2]Department of Chemistry, University of Science and Technology of China, Hefei, Anhui 230026, China

[3]Hefei National Research Center for Physical Sciences at the Microscale, University of Science and Technology of China, Hefei, Anhui 230026, China

[4]Clean Nano Energy Center, State Key Laboratory of Metastable Materials Science and Technology, Yanshan University, Qinhuangdao 066004, China

[5]Multi-scale Porous Materials Center, Institute of Advanced Interdisciplinary Studies & School of Chemistry and Chemical Engineering, Chongqing University, Chongqing 400044, China

[6]National Synchrotron Radiation Laboratory, University of Science and Technology of China, Hefei, Anhui 230026, China

[7]Lead contact

*Correspondence: zyli@ustc.edu.cn (Z.L.), jianglab@ustc.edu.cn (H.-L.J.), weichen1@ustc.edu.cn (W.C.)

https://doi.org/10.1016/j.joule.2023.02.010

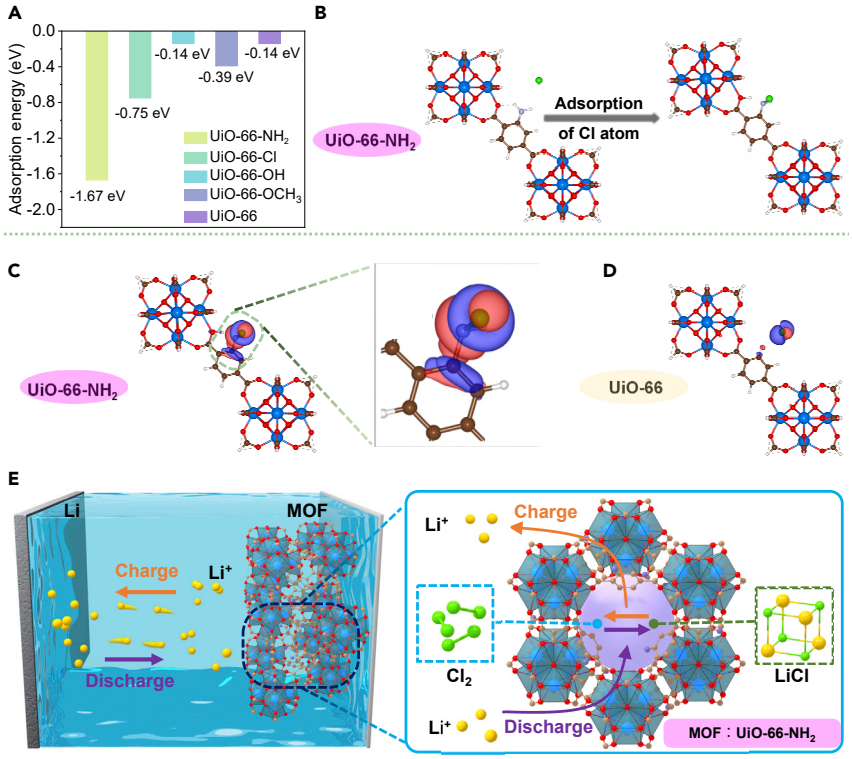

Figure 1. The prediction of functional MOFs for Li-Cl_2 batteries

(A) DFT calculation of adsorption energy of UiO-66-NH_2, UiO-66-Cl, UiO-66-OH, UiO-66-OCH_3, and UiO-66 to Cl atoms.

(B–D) (B) DFT calculation of adsorption process of UiO-66-NH_2 to Cl atoms. The charge density plot of (C) UiO-66-NH_2 and (D) UiO-66 to Cl atoms. Atoms of Zr, O, C, N, and H are colored in blue, red, brown, blue gray, and white, respectively.

(E) Schematic diagram of the Li-Cl_2@MOF (UiO-66-NH_2) cell and the cathode Cl_2/LiCl reaction mechanism.

and UiO-66-OCH_3 to Cl atom were −0.14, −1.67, −0.75, −0.14, and −0.39 eV, respectively, which indicates that the –NH_2 group has the strongest adsorption preference to the Cl atom. Therefore, UiO-66-NH_2 MOF was selected for the Li-Cl_2 battery in this work. Considering that the unit cells of UiO-66 with 440 atoms and UiO-66-NH_2 with 488 atoms are large, a part of the structure, which contains one benzene ring and two roundish $Zr_6O_8(COO)_{12}$ clusters (Figure S2), was taken into investigation for the adsorption of Cl. For the Cl atom adsorption process in UiO-66-NH_2 MOF, Cl can spontaneously occupy the H position of the –NH_2 group and push it to the neighboring O (Figure 1B). By contrast, as depicted in Figure S3, Cl stays at the non-bonded state in UiO-66 when the –NH_2 group is absent. The state of chemical bond formation can be verified by the charge density difference plot in Figures 1C and 1D, where the charge transfer locates at the space between Cl–N–C in UiO-66-NH_2, whereas the charge transfer region is limited around Cl in UiO-66, further indicating the strong chemisorption between –NH_2 group and Cl. Therefore, the existence of the -NH_2 groups in UiO-66-NH_2 can effectively enhance the adsorption of Cl, which is believed to promote the LiCl/Cl_2 reactions in the Li-Cl_2 batteries.

The structure of the Li-Cl_2@MOF cell was depicted in Figure 1E, in which a Li metal anode, a porous UiO-66-NH_2 MOF cathode, and a Li^+-conductive electrolyte were composed. The highly porous UiO-66-NH_2 MOF functionalized with the –NH_2

groups was synthesized based on a previous report with some modifications.[30] Due to the affinity of UiO-66-NH_2 MOF to Cl_2 and LiCl molecules, its storage capacity to Cl_2 and LiCl molecules can be much enhanced. During the first discharge process, Li metal dissolves into Li^+ ions on the anode and $SOCl_2$ solvent is decomposed into a solid product of LiCl ($2SOCl_2 + 4Li^+ + 4e^- \rightarrow SO_2 + S + 4LiCl$), which is stored in the micropores of the UiO-66-NH_2 MOF cathode. During the recharge process, Li^+ ions in the electrolyte deposit onto the Li metal, and LiCl is oxidized to Cl_2, which is stored in the micropores by the chemisorption between the Cl_2 and $-NH_2$ groups in the UiO-66-NH_2 cathode. In the following discharge process, Cl_2 is reduced to LiCl ($1/2Cl_2 + e^- \rightarrow Cl^-$) to complete the battery cycling.

Characterization of pristine UiO-66-NH_2 MOF

Different characterization tools were applied to investigate the functional MOFs. The synthesized UiO-66-NH_2 was first confirmed by X-ray diffraction (XRD). As shown in Figure 2A, all patterns match very well with the UiO-66 MOF. Furthermore, the morphology and structure of pristine UiO-66-NH_2 were characterized by cryo-TEM and its electron diffraction pattern. As shown in Figure 2B, the UiO-66-NH_2 showed an octahedral nanoparticular structure with particle size in the range of 300–600 nm. The inset image showed a typical electron diffraction pattern of the crystal along the <110> zone axis. The sharp diffraction spots of the pristine UiO-66-NH_2 indicated the good crystallinity of the UiO-66-NH_2 sample. In addition, (111) and (002) planes of the crystalline UiO-66-NH_2, which are two of the strongest peaks in the XRD pattern of UiO-66-NH_2 (Figure 2A), further indicate the successful synthesis of UiO-66-NH_2. The lattice planes of (113), (133), (024), (224), and (135) in UiO-66-NH_2 can be detected by electron diffraction in different areas (Figure S4). Moreover, the porous structure of UiO-66-NH_2 was characterized by N_2 adsorption/desorption at 77 K, which exhibited a sharp increase at a low relative pressure ($P/P_0 < 0.05$) and, then, a platform characteristic of the type-I isotherms (Figure 2C). The fitted pore size of UiO-66-NH_2 from the N_2 adsorption isotherm was calculated to be 1.2 nm (Figure 2D), illustrating its microporous feature. The Brunauer–Emmett–Teller (BET) surface area of UiO-66-NH_2 was as high as 1,036 m^2/g. The porous structure and large surface area in UiO-66-NH_2 can provide ample reaction sites for LiCl and Cl_2 redox reactions.

It is well-recognized that the characterization of MOFs at the atomic level is extremely difficult due to their electron-beam sensitivity. In our work, HRTEM images were obtained under an extremely low-dose condition (Figure 2E). Using a 0.03 e/$Å^2$/s cumulative electron dose, we have caught the structural features of UiO-66-NH_2 (Figure 2E), which is hard to be obtained by room temperature TEM. Figure 2E is a representative denoised low-dose HRTEM image of UiO-66-NH_2 along the <110> direction. To make the image contrast more interpretable, contrast transfer function (CTF) correction was performed according to the method reported in the previous literature.[31] In the CTF-corrected image of the pristine UiO-66-NH_2 (Figure 2F), Zr_6O_8 clusters are clearly identified, which is in good agreement with UiO-66-NH_2 crystal structure from the <110> direction. Interestingly, we found the missing linkers in this image, but the contrasts of the horizontally arranged ligands are not presented. As a consequence, the adjacent opposing triangle-shaped channels are vertically merged into rhombus-shaped channels, indicating the rich defects in the UiO-66-NH_2 structure.

Electrochemical performance of the Li-Cl_2@MOF cell at room temperature

In light of the reaction mechanism of Cl_2/LiCl redox in UiO-66-NH_2, a Li-Cl_2@MOF cell was assembled to evaluate the effect of UiO-66-NH_2 on the conversion reactions

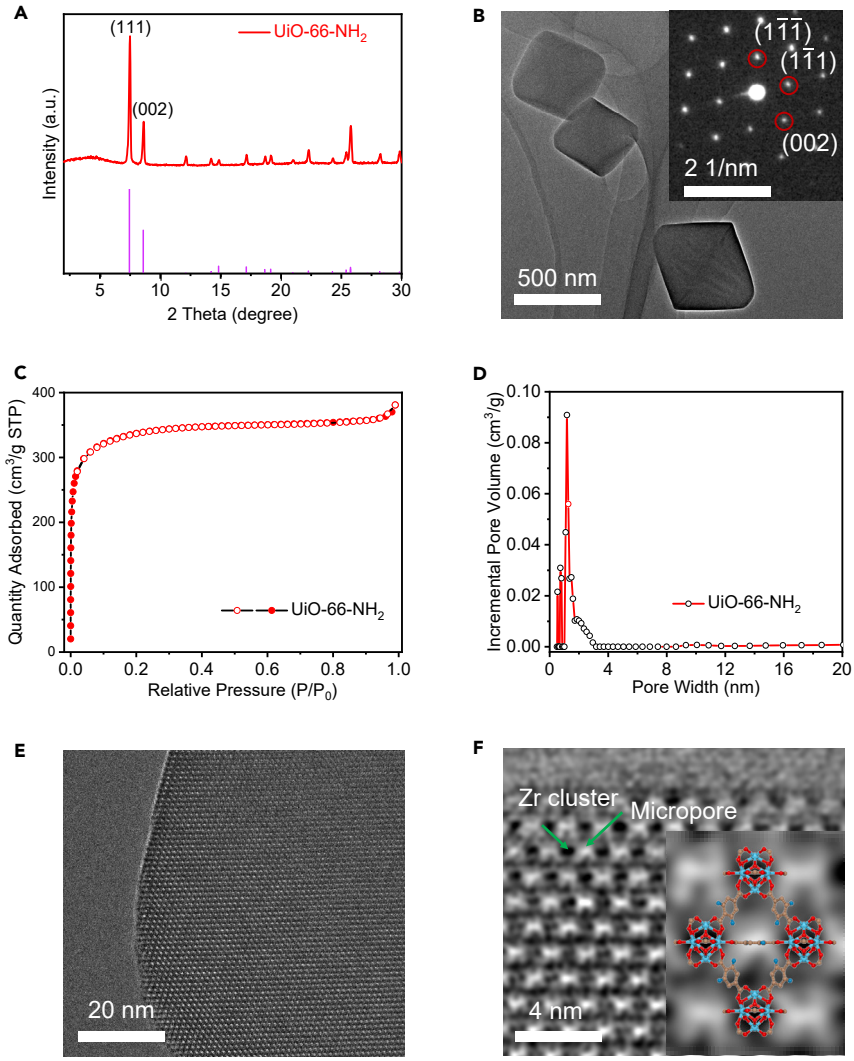

Figure 2. Materials characterizations of UiO-66-NH_2 as a functional MOF for Li-Cl_2 batteries

(A) XRD of pristine UiO-66-NH_2.

(B) Cryo-TEM of pristine UiO-66-NH_2. Inset: electron diffraction pattern of pristine UiO-66-NH_2. Scale bar: 500 nm. Inset scale bar: 2 1/nm.

(C) N_2 gas adsorption/desorption isotherms at 77 K.

(D) The fitted pore size of UiO-66-NH_2 from N_2 adsorption/desorption isotherm.

(E) Low-dose HRTEM image of pristine UiO-66-NH_2. Scale bar: 20 nm.

(F) CTF-corrected image from (E). Inset: A UiO-66-NH_2 model. Orange, red, blue, and cyan spheres represent C, O, N, and Zr atoms, respectively. Scale bar: 4 nm.

of LiCl and Cl_2. First, the UiO-66-NH_2 electrode was characterized by scanning electron microscopy (SEM) and the corresponding energy dispersive X-ray spectroscopy (EDX). As shown in Figures S5 and S6, the UiO-66-NH_2 MOF was uniformly distributed on the conductive carbon, as the C, N, O, and Zr elements were evenly distributed. As shown in Figure S7, the first cycle discharge capacity of the assembled Li-Cl_2@MOF cell was as high as 7,550 mAh/g, which is much superior to the reported literature (3,309 mAh/g).[4] The improved first cycle-specific capacity indicated the much-improved active sites of UiO-66-NH_2 to accommodate LiCl. Furthermore, a high capacity of 1,000 mAh/g was used to charge the Li-Cl_2@MOF cell to evaluate the storage capacity of UiO-66-NH_2. The Li-Cl_2@MOF cell exhibited a long cycle

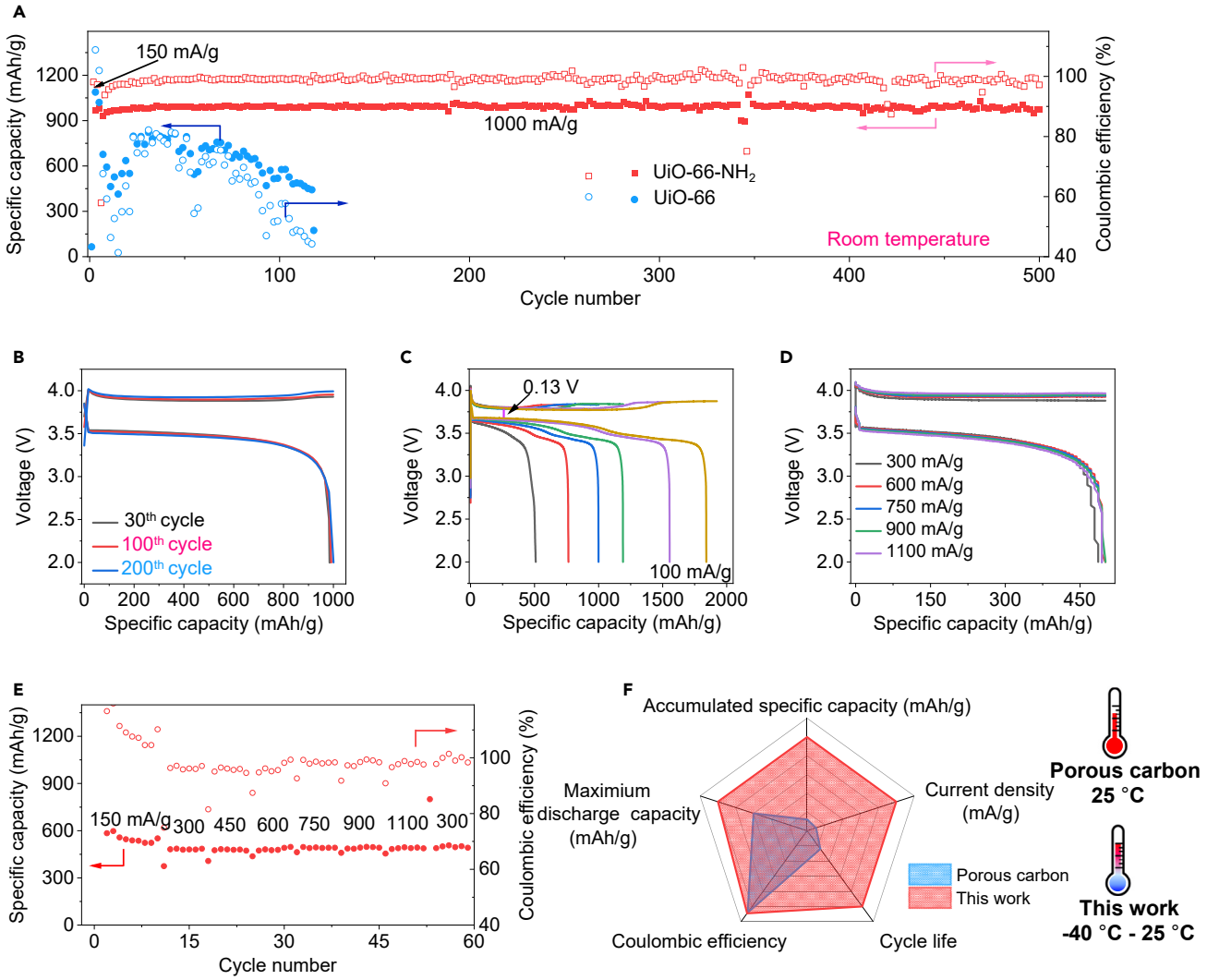

Figure 3. Electrochemical performance of the Li-Cl_2@MOF battery at room temperature

(A) Cycling performance of Li-Cl_2@MOF cells at a current density of 1,000 mA/g.

(B) Corresponding voltage profiles of the Li-Cl_2@MOF cell in different cycles.

(C) Voltage profiles of the Li-Cl_2@MOF cell under the specific capacities from 500 to 2,000 mAh/g.

(D and E) (D) Voltage profiles and (E) Cycling performance of the Li-Cl_2@MOF cell under the current densities from 150 to 1,100 mA/g.

(F) Comparison of this work with the previously reported porous carbon in terms of accumulated specific capacity, current density, cycle life, working temperature range, Coulombic efficiency, and maximum specific capacity.

stability of over 500 cycles and a high output specific capacity of 980 mAh/g after 500 cycles with a high cycling CE up to ~99.7% (Figure 3A), indicating the excellent storage capacity of UiO-66-NH_2 and the superb stability of its structure. Additionally, an ultra-flat discharge voltage plateau was well maintained within 200 cycles at 3.5 V (Figure 3B), further suggesting the high stability of the UiO-66-NH_2 structure. To investigate the importance of the –NH_2 groups, UiO-66 containing no such –NH_2 groups was used as a control sample to assemble the Li-Cl_2 battery. As shown in Figure 3A, the specific capacity of the Li-Cl_2 cell using UiO-66 fades to merely 600 mAh/g within only 10 cycles, indicating its limited Cl_2/LiCl conversion capability due to the lack of the –NH_2 groups to trap Cl_2 and LiCl. Furthermore, the Li-Cl_2 cell was assembled using ketjenblack as the cathode. As shown in

Figure S8, although the BET surface area of ketjenblack was as high as 1,348 m^2/g, the CE of the Li-Cl_2 cell was merely 95% at the initial cycles, which dropped dramatically to 74% within 100 cycles and to 54% within 200 cycles at the current density of 450 mA/g, further indicating the importance of the -NH_2 groups in the functional MOF design.

The cycling performance of the Li-Cl_2@MOF cell under different charge capacities was further evaluated. As shown in Figures 3C and S9, the cell was cyclable at 500–2,000 mAh/g, and the CE was maintained at ~100% when the capacity was between 500 and 1,500 mAh/g. Even at the ultra-high capacity of 2,000 mAh/g, the CE still can reach up to 96%. As shown in Figure 3C, the overpotential of Li-Cl_2@MOF cell was as low as 0.13 V with a charge voltage of ~3.80 V and a discharge voltage of ~3.67 V when cycling at the current density of 100 mA/g, further indicating the fast Cl_2/LiCl gas/solid conversion reaction kinetics promoted by the functional MOF structure.

To investigate the reaction kinetics of the Li-Cl_2@MOF cell, the cycling performance of the Li-Cl_2@MOF cell under different current densities was also investigated. When the current density increased from 150 to 1,100 mA/g, the decrease of the discharge voltage plateau was negligible, and the discharge voltages were maintained at ~3.5 V, suggesting the fast reduction kinetics from Cl_2 to LiCl due to the strongly bonded Cl_2 with UiO-66-NH_2 (Figure 3D). Meanwhile, the charge voltage was merely increased from 3.81 to 3.96 V (Figure 3D) when the current density was increased from 150 to 1,100 mA/g, indicating that the oxidation kinetics from LiCl to Cl_2 was also fast due to the strong binding of LiCl with UiO-66-NH_2. As shown in Figure 3E, the Li-Cl_2@MOF cell delivered specific capacities of around 500 mAh/g at the current densities from 300 to 1,100 mA/g, when the charge capacity is 500 mAh/g. It is noted that the CE is a little bit higher than 100% at the first several cycles under a current density of 150 mA/g, which can be ascribed to the extra decomposition of $SOCl_2$ during the initial cell activation process. When charging the battery at a fixed specific capacity of 500 mAh/g, the corresponding CE is maintained at ~100% even at a high current density of 1,100 mA/g. Encouragingly, compared with the reported Li-Cl_2 cell by porous carbon, our Li-Cl_2@MOF cell showed much superior electrochemical performance in the aspects of accumulated specific capacity, current density, and working temperature range, which is summarized in Figure 3F. Specifically, our Li-Cl_2@MOF cell showed a cumulative capacity of up to 500,000 mAh/g, which is about 8 times higher than the reported Li-Cl_2 cell by porous carbon. Particularly, the cycling current density can be improved from 100 to 1,000 mA/g, which is ~10 times higher than the reported Li-Cl_2 cell by porous carbon. In addition, the operating temperature range of our Li-Cl_2@MOF cell was enlarged from −40°C to 25°C, which can be applied to more application situations. These advantages suggest the great promises of the MOFs with functional groups as cathodes for high-energy Li-Cl_2 batteries.

Low-temperature electrochemical behaviors of the Li-Cl_2@MOF cell

To explore the feasibility of the Li-Cl_2@MOF cells to be applied in extreme weather, we carried out their electrochemical performance measurements under low temperatures. Figures 4A and 4B show the electrochemical performance of the Li-Cl_2@MOF cells under temperatures from 0°C to −40°C. At 0°C, the discharge capacity of the Li-Cl_2@MOF cells is about 1,022 mAh/g when the charge capacity was set at 1,000 mAh/g. When the temperature was reduced to −10°C, the Li-Cl_2@MOF cells can provide a high capacity of ~1,000 mAh/g. With the temperature further decreased to −40°C, the Li-Cl_2@MOF cells can still deliver a capacity of 989 mAh/g. The CE can

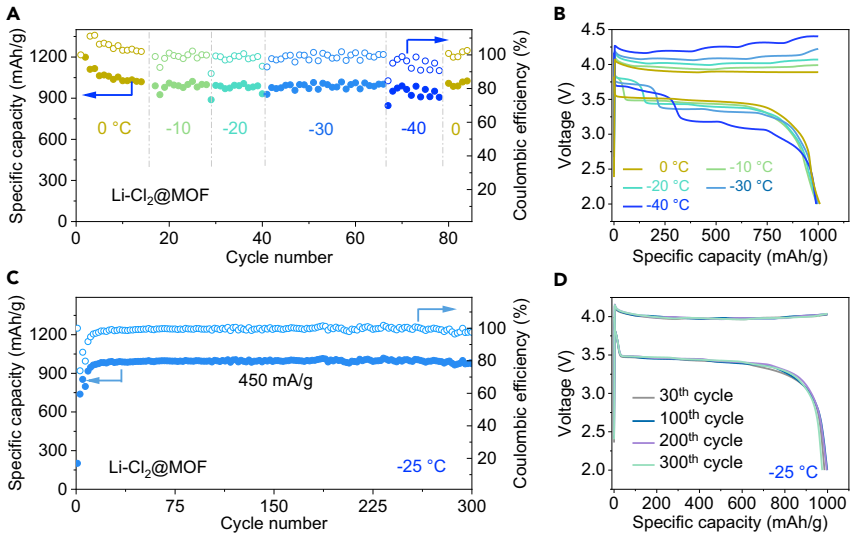

Figure 4. Low-temperature electrochemical performance of Li-Cl_2@MOF batteries

(A and B) (A) Cycling performance and (B) voltage profiles of Li-Cl_2@MOF cell under different temperatures from 0°C to −40°C.

(C and D) (C) Cycling performance and (D) voltage profiles of Li-Cl_2@MOF cell under the temperature of −25°C.

be maintained at ~102%, ~100%, ~99.6%, ~99.7%, and ~98.9% under the temperatures of 0°C, −10°C, −20°C, −30°C, and −40°C, respectively, which indicated the good reversibility of the Li-Cl_2@MOF cells under low temperatures. When the temperature returned to 0°C, the discharge capacity returned to nearly 1,000 mAh/g, suggesting a good temperature tolerance of the Li-Cl_2@MOF cells. The discharge plateau of the Li-Cl_2@MOF cell was 3.50 V at 0°C (Figure 4B), which is comparable with that at room temperature (Figure 3C). When the temperature decreased to −30°C, the discharge plateau merely dropped by 0.14 V, which indicated the reaction kinetics from Cl_2 to LiCl was fast even at low temperatures, further verifying the strong binding of Cl_2 with UiO-66-NH_2. It is worth mentioning that the polarization in the charge process with the temperature decrease was higher than that in the discharge process, which indicated that the solid to gas reaction kinetics from LiCl to Cl_2 is impacted greater by temperature than the gas to solid reaction kinetics from Cl_2 to LiCl. In addition to the excellent rate capability performance, the long-term cycling stability of the Li-Cl_2@MOF cells was also evaluated at −25°C. The Li-Cl_2@MOF cells provide an ultra-high first discharge capacity of 7,190 mAh/g (Figure S10) and a high specific capacity of 996 mAh/g when the charge capacity was set at 1,000 mAh/g for a lifespan of 300 cycles with nearly 100% of the capacity retention (Figure 4C). In addition, the Li-Cl_2@MOF cells showed a maintained discharge plateau of 3.5 V at −25°C within 200 cycles (Figure 4D), which demonstrated their practical long-term application at low temperatures.

Investigation of reaction mechanism of the Li-Cl_2@MOF cell

The reaction mechanism of the –NH_2 groups to the Cl_2/LiCl conversion reactions is illustrated in Figure 5A. Typically, Cl_2 interacted with the –NH_2 groups by chemisorption, spontaneously H atom was pushed to the neighboring O and its position in the –NH_2 groups was occupied (Figure S3). During the discharge process, the bonded Cl_2 was supplied to the reduction reaction to form LiCl, and during the charge process, the formed Cl_2 was trapped by the –NH_2 groups to suppress its shuttle effect. To investigate the reaction mechanism of the improvements by using UiO-66-NH_2 in

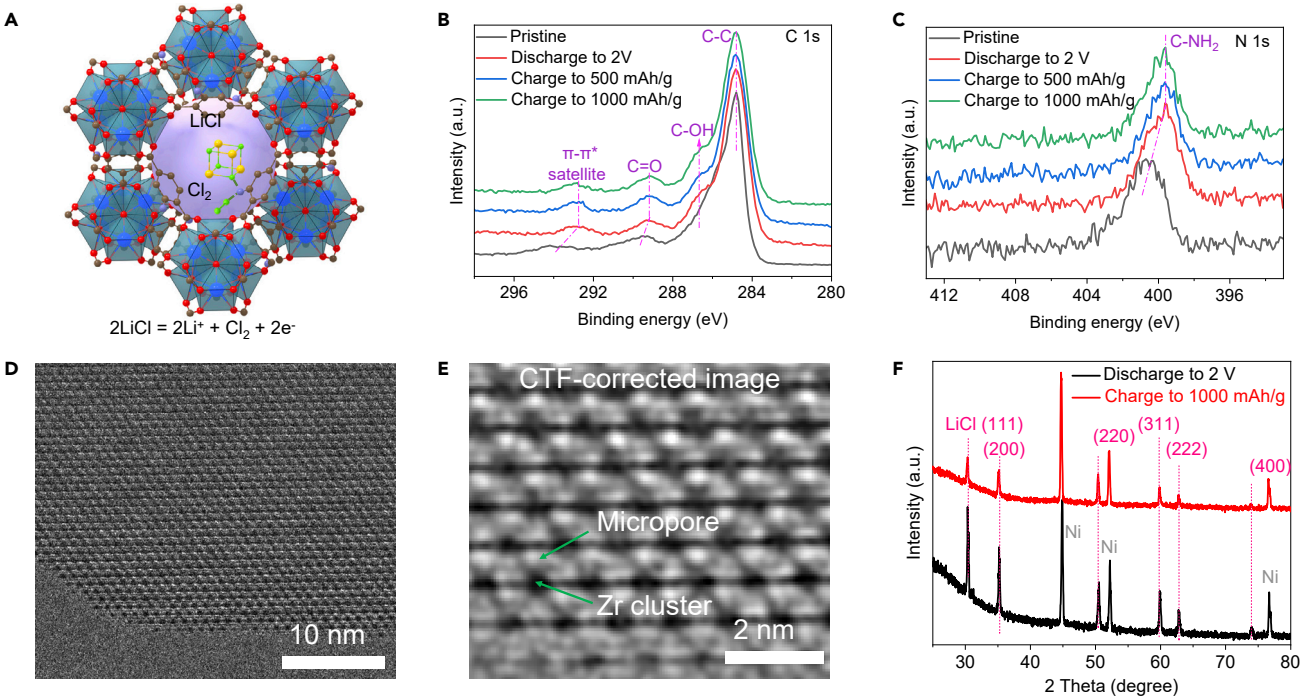

Figure 5. The working mechanism of Li-Cl_2@MOF batteries

(A) The schematic diagram of redox reaction of Cl_2/LiCl.

(B and C) (B) C 1s and (C) N 1s XPS spectra of UiO-66-NH_2 cathode under the states of pristine, discharge to 2 V, charge to 500 mAh/g and charge to 1,000 mAh/g.

(D) Low-dose HRTEM image of UiO-66-NH_2 discharged to 150 mAh/g. Scale bar: 10 nm.

(E) CTF-corrected image from (D). Scale bar: 2 nm.

(F) XRD pattern of UiO-66-NH_2 cathode under the states of discharge to 2 V and charge to 1,000 mAh/g.

the Li-Cl_2 cell, XPS, XRD, and low-dose HRTEM were applied to analyze the cycled UiO-66-NH_2 cathode. XPS was conducted to verify the bond interaction between the Cl atom and UiO-66-NH_2. As shown in Figure 5B, the C 1s spectrum can be deconvoluted into the C–C group (284.8 eV), C–OH group (286.6 eV), C=O group (289.0 eV), and π-π* satellite structure (292.7 eV), in which the π-π* satellite structure is ascribed to the extended delocalized electrons in the aromatic ring. The C–C and C=O groups are ascribed to the carbon in the aromatic ring and carbonyl group of 2-amino-1,4-benzenedicarboxylate. Compared with the pristine UiO-66-NH_2 MOF, the C–C group in the aromatic ring kept unchanged in the UiO-66-NH_2 MOF in the states of discharge to 2 V, charge to 500 mAh/g, and charge to 1,000 mAh/g, which indicated that the electron state in the aromatic ring was negligibly changed when the Cl atom was adsorbed. The C–OH group emerged in the states of discharge to 2 V, charge to 500 mAh/g and charge to 1,000 mAh/g compared with the C–O group in the pristine UiO-66-NH_2, suggesting the proton transfer to the C–O group, which is identical to the computational results. The –NH_2 groups connected to the benzene ring can be detected in the N 1s XPS (400.7 eV) (Figure 5C). Both N 1s peak (400.7 eV) ascribed to the C–NH_2 group and the π-π* satellite peak in C 1s moved to the lower energy after the Cl atom was adsorbed in the states of discharge to 2 V, charge to 500 mAh/g, and charge to 1,000 mAh/g, indicating that the electron on C–NH_2 was transferred to the Cl atom due to the adsorption of Cl_2/LiCl, which is consistent with the computational results. Both the C 1s and N 1s XPS results verified that Cl_2/LiCl bonded with the –NH_2 groups while pushing one proton in the –NH_2 group to the neighboring O in the C–O group.

It is known that the stability of electrode materials significantly affected the battery performance. Thus, we performed low-dose HRTEM imaging of the UiO-66-NH_2 cathode discharged to 150 mAh/g to check its structural stability. As shown in Figure 5D, the crystalline structure of the cycled UiO-66-NH_2 MOF was retained, indicating stable and reliable characteristics of UiO-66-NH_2 MOF in the Li-Cl_2 cell. The CTF-corrected image obtained from Figure 5D further verified that the channel structure was maintained in the cycled UiO-66-NH_2 MOF (Figure 5E). XRD was conducted on UiO-66-NH_2 MOF in the same state, but no peak shift can be observed (Figure S11), further indicating the stability of UiO-66-NH_2 MOF. The discharge products in the UiO-66-NH_2 cathode under the states of discharge to 2 V and charge to 1000 mAh/g were investigated by XRD. As shown in Figure 5F, the diffraction peaks of 30.3°, 35.2°, 50.4°, 60°, 62.8°, and 73.4° can be assigned to the (111), (200), (220), (311), (222), and (400) planes of LiCl, respectively, which indicated the formation of crystalline LiCl. In light of the XPS, XRD, and low-dose HRTEM results, we identified that both the highly porous structure and the stable functional group are responsible for boosting the electrochemical performance of the Li-Cl_2 cell.

Electrochemical performance of the Li-Cl_2@MOF pouch cell

To meet the requirements for the practical application, the Li-Cl_2@MOF cell in large areal capacity was assembled in the coin-type cell. As shown in Figure 6A, the Li-Cl_2@MOF cell showed a stable performance up to 150 cycles at a high areal capacity of 4.4 mAh/cm^2 with a negligible capacity degradation, which indicated the superb capability of the UiO-66-NH_2 MOF to the Cl_2 and LiCl reactions. To further demonstrate the superiority of our Li-Cl_2@MOF cell, large-scale pouch cells were assembled with an electrode area of 20 cm^2 (4.0 cm × 5.0 cm). The as-prepared pouch cell was cycled at a current density of 150 mA/g with a charge capacity of 38 mAh (Figure 6B). Under such conditions, the pouch cell delivered over 120 stable cycles, and the Coulombic efficiency can be maintained over 99%. It is worth mentioning that the voltage profiles of the pouch cell showed a similar discharge plateau at 3.64 V to the coin cell (Figure 6C), demonstrating its promising practical utilization. Although the Li-Cl_2@MOF pouch cell showed advantages in the discharge voltage, output specific capacity, and cycle stability compared with other Li-based batteries, the electrolyte utilization should be further optimized, and cell engineering is needed to tackle the corrosion issues of $SOCl_2$ and Cl_2.

Conclusion

In conclusion, we applied the first-principles calculations to predict UiO-66-NH_2 as a functional MOF to be used as a cathode material in the rechargeable Li-Cl_2 batteries, in which the highly stable, porous structure and functional groups are critical to boost the battery electrochemical performance. The working mechanism of the UiO-66-NH_2 MOF structure to enrich the Cl_2/LiCl reactions was revealed by a combination of cryo-TEM, low-dose HRTEM and XPS. Our designed Li-Cl_2@MOF full cell showed high capacities of up to 2,000 mAh/g and over 500 stable cycles at a specific capacity of 1,000 mAh/g at room temperature. The Li-Cl_2@MOF cell also exhibited excellent electrochemical performance at low temperatures, delivering a maintained CE of 99.7% with a discharge plateau of 3.5 V and 300 stable cycles under a capacity of 1,000 mAh/g at −25°C. Moreover, the Li-Cl_2@MOF cells achieved a high areal capacity of 4.4 mAh/cm^2 and a large-scale pouch cell fabrication, showing their practical energy storage applications. This study opens new avenues to the development of rechargeable Li-Cl_2 batteries with high capacity and excellent stability under a wide temperature range. However, the exploration of rechargeable Li-Cl_2 batteries is still in its very early stage, and further

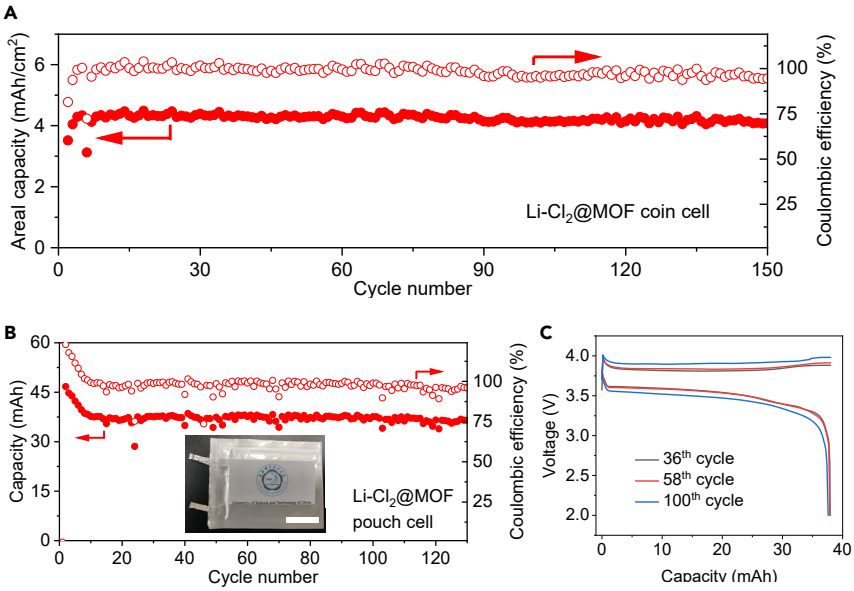

Figure 6. Electrochemical performance of the Li-Cl_2@MOF pouch cell

(A) The cycling stability of Li-Cl_2@MOF cell at a large areal capacity of 4.4 mAh/cm^2.

(B) Cycling performance and (C) voltage profiles of the Li-Cl_2@MOF pouch cell with a charge capacity of 38 mAh at a current density of 150 mA/g. Scale bar in (B), 2 cm.

optimizations are needed to enhance the practical energy density for widespread applications.

EXPERIMENTAL PROCEDURES

Resource availability

Lead contact

Further information and requests for resources and materials should be directed to and will be fulfilled by the lead contact, Wei Chen (Weichen1@ustc.edu.cn).

Materials availability

This study did not generate new unique materials.

Synthesis of UiO-66-NH_2. UiO-66-NH_2 was synthesized according to a previously reported study.[32] In brief, zirconium tetrachloride ($ZrCl_4$, 1.5 g), 2-amino-1,4-benzenedicarboxylic acid (NH_2-BDC, 1.07 g), acetic acid (CH_3COOH, 44 mL), and deionized water (7.5 mL) were added into dimethylformamide (DMF, 100 mL) and then reacted at 120°C for 15 min under vigorous stirring in an oil bath. The as-synthesized UiO-66-NH_2 was washed with DMF and methanol in sequence. Finally, the resulting product, which is a yellow solid, was dried overnight at 60°C under vacuum.

Preparation of electrolyte. The electrolyte was prepared according to a reported study by Zhu et al.[4] Briefly, 1.088 g $AlCl_3$ with 4 wt % LiTFSI and 4 wt % LiFSI were added into a 20 mL vial, and then 2 mL $SOCl_2$ was added and stirred for 5 min. Finally, a light-yellow solution can be obtained.

Li-Cl_2@MOF coin cell assembly. The nonaqueous Li-Cl_2@MOF coin-type battery was assembled in an Ar-filled glovebox with O_2 and H_2O concentrations under 0.3 ppm. Lithium foil was used as anode, and a volume of 100 μL electrolyte was added

with glass fiber separator. The cathodes were prepared by mixing 60 mg UiO-66-NH_2 MOF, 30 mg ketjenblack, and 10 mg poly(tetrafluoroethylene) (PTFE) dissolved in alcohol to form a slurry. The resulting slurry was uniformly drop casted onto Ni foam, and then the cathode was dried in an oven at 60°C for 12 h. The mass loading of the cathode active material is in the range of 0.7–5 mg/cm^2. The electrochemical performance of the cells at low temperature and room temperature were tested on the Neware and Landt battery testing systems, respectively.

Li-Cl_2@MOF pouch cell assembly. The pouch cells were assembled in a dry room. The Ni foam substrate was used as the current collector for cathode and anode with an area of 20 cm^2 (4.0 cm × 5.0 cm). Ni tabs were welded with Ni foam by ultrasonic welding for 1.2 s. The slurry consisting of UiO-66-NH_2 MOF, ketjenblack, and PTFE in a mass ratio of 6:3:1 was drop casted onto Ni foam and then dried in an oven at 60°C for 12 h. The mass loading of active material is in the range of 45–56 mg. Li foil was pressed onto the Ni foam directly. The glass fiber separator was cut into pieces of 5.0 cm × 6.0 cm. The anode, separator, and cathode were stacked up in sequence, and insulating taps were applied to immobilize the electrodes. It is worth to mention that glass plates were placed between aluminum-plastic film and electrode to avoid any possible corrosion of the electrolyte to the aluminum-plastic film. Then the cell was transferred to an Ar-filled glovebox to inject electrolyte. 2.2 mL of electrolyte was added in each pouch cell, and it was finally heating sealed.

Characterizations. Powder X-ray diffraction (PXRD) patterns were characterized by a Japan Rigaku MiniFlex 600 equipped with graphite-monochromated Cu K_α radiation. Scanning electron microscope (SEM, JEOL-6700F) was used to characterize the morphologies and EDX of pristine and cycled UiO-66-NH_2 cathode. Valence state measurements were obtained by X-ray photoelectron spectroscopy (XPS) equipped with a monochromatic Al K_α source. Room temperature TEM characterizations were carried out using an Cs-corrected environmental transmission electron microscope (ETEM, FEI Titan G2) operated at 300 kV and all cryo-EM experiments were performed on the same instrument with a Fischione sample holder. Low-dose TEM characterizations were carried out using an Cs-corrected transmission electron microscope (FEI Titan) operated at 300 kV. The sample searching, the alignment of crystal zone axis, and prefocusing were performed at a 13,000× magnification with a dose rate of about 0.03 e/$Å^2$/s. The HRTEM images were obtained by utilizing a Gatan K3 direct-detection camera in the electron-counting mode. The total electron dose used for each image was controlled within 15 e/$Å^2$ to avoid structural damage of the samples. The images were finely processed via CTF correction to be more directly interpretable.

Theoretical calculations. Spin-polarized density functional theory calculations were performed by Vienna Ab-initio Simulation Package (VASP)[33,34] using projector-augmented wave (PAW) pseudopotentials[35] and Perdew-Burke-Ernzerhof (PBE) functional.[36] Electrons in the states of (4s, 4p, 5s, and 4d) of Zr, (1s) of H, (2s and 2p) of C and O were considered valence electrons. The cutoff energy of the plane-wave basis was set to be 520 eV. Considering that the unit cells of Ui-66 with 440 atoms and Ui-66-NH_2 with 488 atoms are extremely large, a part of the structure, which contains one benzene ring and two roundish $Zr_6O_8(COO)_{12}$ clusters (Figure S2), was cut to investigate the adsorption of Cl. The cut site was passivated with additional H atoms. This part of structure was simulated in a 40 × 40 × 40 $Å^3$ cubic box with enough vacuum region, and a single gamma k-point was used. There are 64 O, 30 C, 12 Zr, and 26 H atoms in the UiO-66 system, whereas one H on benzene ring was replaced by the –NH_2 group in the UiO-66-NH_2 system. The

convergence for electronic energy and structural optimization was set to be $1E^{-5}$ eV and 0.02 eV/Å, respectively.

Data and code availability

The data and code presented in this work are available from the corresponding authors upon reasonable request.

SUPPLEMENTAL INFORMATION

Supplemental information can be found online at https://doi.org/10.1016/j.joule.2023.02.010.

ACKNOWLEDGMENTS

The work was supported by the Fundamental Research Funds for the Central Universities (grant WK2060000040, KY2060000150, and 2022CDJXY-003), the China Postdoctoral Science Foundation (2021M693061), and the National Natural Science Foundation of China (21825302 and 22105028). We acknowledge the support from the USTC Center for Micro and Nanoscale Research and Fabrication, the USTC Supercomputer Center, and BL11U beamline in the National Synchrotron Radiation Laboratory (NSRL) in Hefei, China.

AUTHOR CONTRIBUTIONS

Y.X. and W.C. conceived the idea and designed the experiments. Y.X. performed the experiments of the main research and wrote the manuscript under the guidance of W.C. L.J. and H.-L.J. synthesized the MOF materials. J.M. and Z.L. performed the theoretical calculations. P.Z., Y.T., L.L., and Y.L. conducted and analyzed the TEM data. H.D., J.S., and M.W. participated in the discussion of the experimental details and the framework of the work.

DECLARATION OF INTERESTS

A patent application based on this work has been filed.

Received: December 14, 2022
Revised: January 18, 2023
Accepted: February 15, 2023
Published: March 15, 2023

REFERENCES

1. Chu, S., and Majumdar, A. (2012). Opportunities and challenges for a sustainable energy future. Nature *488*, 294–303. https://doi.org/10.1038/nature11475.

2. Armand, M., and Tarascon, J.M. (2008). Building better batteries. Nature *451*, 652–657. https://doi.org/10.1038/451652a.

3. Zhu, Z., Jiang, T., Ali, M., Meng, Y., Jin, Y., Cui, Y., and Chen, W. (2022). Rechargeable batteries for grid scale energy storage. Chem. Rev. *122*, 16610–16751. https://doi.org/10.1021/acs.chemrev.2c00289.

4. Zhu, G., Tian, X., Tai, H.C., Li, Y.Y., Li, J., Sun, H., Liang, P., Angell, M., Huang, C.L., Ku, C.S., et al. (2021). Rechargeable Na/Cl_2 and Li/Cl_2 batteries. Nature *596*, 525–530. https://doi.org/10.1038/s41586-021-03757-z.

5. Zhu, G., Liang, P., Huang, C.L., Huang, C.C., Li, Y.Y., Wu, S.C., Li, J., Wang, F., Tian, X., Huang, W.H., et al. (2022). High-capacity rechargeable Li/Cl_2 batteries with graphite positive electrodes. J. Am. Chem. Soc. *144*, 22505–22513. https://doi.org/10.1021/jacs.2c07826.

6. Xia, M., Feng, Y., Wei, J., Rao, A.M., Zhou, J., and Lu, B. (2022). A rechargeable K/Br battery. Adv. Funct. Mater. *32*, 2205879. https://doi.org/10.1002/adfm.202205879.

7. Zhao, R., Liang, Z., Zou, R., and Xu, Q. (2018). Metal-organic frameworks for batteries. Joule *2*, 2235–2259. https://doi.org/10.1016/j.joule.2018.09.019.

8. Ye, Z., Jiang, Y., Li, L., Wu, F., and Chen, R. (2021). Rational design of MOF-based materials for next-generation rechargeable batteries. Nanomicro Lett. *13*, 203. https://doi.org/10.1007/s40820-021-00726-z.

9. Liang, Z., Qu, C., Guo, W., Zou, R., and Xu, Q. (2018). Pristine metal-organic frameworks and their composites for energy storage and conversion. Adv. Mater. *30*, e1702891. https://doi.org/10.1002/adma.201702891.

10. Peng, Y., Wei, X., Wang, Y., Li, W., Zhang, S., and Jin, J. (2022). Metal-organic framework composite photothermal membrane for removal of high-concentration volatile organic compounds from water via molecular sieving. ACS Nano *16*, 8329–8337. https://doi.org/10.1021/acsnano.2c02520.

11. Hou, C.-C., and Xu, Q. (2019). Metal-organic frameworks for energy. Adv. Energy Mater. *9*, 1801307. https://doi.org/10.1002/aenm.201801307.

12. Li, Z., Ge, X., Li, C., Dong, S., Tang, R., Wang, C., Zhang, Z., and Yin, L. (2020). Rational microstructure design on metal-organic

framework composites for better electrochemical performances: design principle, synthetic strategy, and promotion mechanism. Small Methods *4*, 1900756. https://doi.org/10.1002/smtd.201900756.

13. Wu, D., Guo, Z., Yin, X., Pang, Q., Tu, B., Zhang, L., Wang, Y.G., and Li, Q. (2014). Metal–organic frameworks as cathode materials for Li-O_2 batteries. Adv. Mater. *26*, 3258–3262. https://doi.org/10.1002/adma.201305492.

14. Li, Q., Xu, P., Gao, W., Ma, S., Zhang, G., Cao, R., Cho, J., Wang, H.L., and Wu, G. (2014). Graphene/graphene-tube nanocomposites templated from cage-containing metal-organic frameworks for oxygen reduction in Li-O_2 batteries. Adv. Mater. *26*, 1378–1386. https://doi.org/10.1002/adma.201304218.

15. Dou, Y., Lian, R., Zhang, Y., Zhao, Y., Chen, G., Wei, Y., and Peng, Z. (2018). Co_9S_8@carbon porous nanocages derived from a metal–organic framework: a highly efficient bifunctional catalyst for aprotic Li-O_2 batteries. J. Mater. Chem. A *6*, 8595–8603. https://doi.org/10.1039/C8TA01913D.

16. Zeng, Q., Li, X., Gong, W., Guo, S., Ouyang, Y., Li, D., Xiao, Y., Tan, C., Xie, L., Lu, H., et al. (2022). Copolymerization of sulfur chains with vinyl functionalized metal−organic framework for accelerating redox kinetics in lithium-sulfur batteries. Adv. Energy Mater. *12*, 2104074. https://doi.org/10.1002/aenm.202104074.

17. Zhu, J.P., Wang, X.H., and Zuo, X.X. (2019). The application of metal-organic frameworks in electrode materials for lithium-ion and lithium-sulfur batteries. R. Soc. Open Sci. *6*, 190634. https://doi.org/10.1098/rsos.190634.

18. Jiang, H., Liu, X.C., Wu, Y., Shu, Y., Gong, X., Ke, F.S., and Deng, H. (2018). Metal-organic frameworks for high charge-discharge rates in lithium-sulfur batteries. Angew. Chem. Int. Ed. Engl. *57*, 3916–3921. https://doi.org/10.1002/anie.201712872.

19. Meng, J., Liu, X., Niu, C., Pang, Q., Li, J., Liu, F., Liu, Z., and Mai, L. (2020). Advances in metal-organic framework coatings: versatile synthesis and broad applications. Chem. Soc. Rev. *49*, 3142–3186. https://doi.org/10.1039/C9CS00806C.

20. Demir-Cakan, R., Morcrette, M., Nouar, F., Davoisne, C., Devic, T., Gonbeau, D., Dominko, R., Serre, C., Férey, G., and Tarascon, J.M. (2011). Cathode composites for Li-S batteries via the use of oxygenated porous architectures. J. Am. Chem. Soc. *133*, 16154–16160. https://doi.org/10.1021/ja2062659.

21. Bai, S., Liu, X., Zhu, K., Wu, S., and Zhou, H. (2016). Metal-organic framework-based separator for lithium–sulfur batteries. Nat. Energy *1*, 16094. https://doi.org/10.1038/nenergy.2016.94.

22. Gao, G.K., Wang, Y.R., Wang, S.B., Yang, R.X., Chen, Y., Zhang, Y., Jiang, C., Wei, M.J., Ma, H., and Lan, Y.Q. (2021). Stepped channels integrated lithium-sulfur separator via photoinduced multidimensional fabrication of metal-organic frameworks. Angew. Chem. Int. Ed. Engl. *60*, 10147–10154. https://doi.org/10.1002/anie.202016608.

23. Tian, M., Pei, F., Yao, M., Fu, Z., Lin, L., Wu, G., Xu, G., Kitagawa, H., and Fang, X. (2019). Ultrathin MOF nanosheet assembled highly oriented microporous membrane as an interlayer for lithium-sulfur batteries. Energy Storage Materials *21*, 14–21. https://doi.org/10.1016/j.ensm.2018.12.016.

24. Ding, M., Flaig, R.W., Jiang, H.L., and Yaghi, O.M. (2019). Carbon capture and conversion using metal-organic frameworks and MOF-based materials. Chem. Soc. Rev. *48*, 2783–2828. https://doi.org/10.1039/C8CS00829A.

25. Soni, S., Bajpai, P.K., and Arora, C. (2020). A review on metal-organic framework: synthesis, properties and application. Charact. Appl. Nanomater. *2*, 87–102. https://doi.org/10.24294/can.v2i2.551.

26. Ali Akbar Razavi, S., and Morsali, A. (2019). Linker functionalized metal-organic frameworks. Coord. Chem. Rev. *399*, 213023. https://doi.org/10.1016/j.ccr.2019.213023.

27. Morsali, A., and Razavi, A.A. (2020). Functional Metal-Organic Frameworks by Oxygen and Sulfur Based Functions (John Wiley & Sons, Ltd), pp. 133–164.

28. Cao, L., Lv, F., Liu, Y., Wang, W., Huo, Y., Fu, X., Sun, R., and Lu, Z. (2015). A high performance O_2 selective membrane based on CAU-1-NH_2@polydopamine and the PMMA polymer for Li-air batteries. Chem. Commun. (Camb) *51*, 4364–4367. https://doi.org/10.1039/C4CC09281C.

29. Flaig, R.W., Osborn Popp, T.M., Fracaroli, A.M., Kapustin, E.A., Kalmutzki, M.J., Altamimi, R.M., Fathieh, F., Reimer, J.A., and Yaghi, O.M. (2017). The chemistry of CO_2 capture in an amine-functionalized metal–organic framework under dry and humid conditions. J. Am. Chem. Soc. *139*, 12125–12128. https://doi.org/10.1021/jacs.7b06382.

30. He, T., Xu, X., Ni, B., Wang, H., Long, Y., Hu, W., and Wang, X. (2017). Fast and scalable synthesis of uniform zirconium-, hafnium-based metal-organic framework nanocrystals. Nanoscale *9*, 19209–19215. https://doi.org/10.1039/C7NR06274E.

31. Zhang, D., Zhu, Y., Liu, L., Ying, X., Hsiung, C.E., Sougrat, R., Li, K., and Han, Y. (2018). Atomic-resolution transmission electron microscopy of electron beam-sensitive crystalline materials. Science *359*, 675–679. https://doi.org/10.1126/science.aao0865.

32. Ai, Z., Jiao, L., Wang, J., and Jiang, H.-L. (2022). Generation of Hierarchical Pores in Metal–Organic Frameworks by Introducing Rigid Modulator. CCS Chemistry *4*, 3705–3714. https://doi.org/10.31635/ccschem.022.202201974.

33. Kresse, G. (1996). Efficiency of ab-initio total energy calculations for metals and semiconductors using a plane-wave basis set. J. Comput. Mater. Sci. *6*, 15–50. https://doi.org/10.1016/0927-0256(96)00008-0.

34. Kresse, G. (1996). Efficient iterative schemes for ab initio total-energy calculations using a plane-wave basis set. Phys. Rev. B. *54*, 11169–11186. https://doi.org/10.1103/physrevb.54.11169.

35. Kresse, G., and Joubert, D. (1999). From ultrasoft pseudopotentials to the projector augmented-wave method. Phys. Rev. B. *59*, 1758–1775. https://doi.org/10.1103/PhysRevB.59.1758.

36. Perdew, J.P., Burke, K., and Ernzerhof, M. (1996). Generalized Gradient Approximation Made Simple. Phys. Rev. Lett. *77*, 3865–3868. https://doi.org/10.1103/PhysRevLett.77.3865.